Dynamo action in an annular array of helical vortices

R. Volk, P. Odier, and J.-F. Pinton
Laboratoire de Physique, CNRS UMR#5672, École Normale Supérieure de Lyon, 46 Allée d'Italie, F-69007 Lyon, France

(Received 27 March 2007; accepted 27 November 2007; published online 18 January 2008)

We numerically study the induction mechanisms generated from an array of helical motions distributed along a cylinder. Our flow is a very idealized geometry of the columnar structure that has been proposed for the convective motion inside the Earth's core. Using an analytically prescribed flow, we apply a recently introduced iterative numerical scheme [M. Bourgoin, P. Odier, J.-F. Pinton, and Y. Richard, Phys. Fluids **16**, 2529 (2004)] to solve the induction equation and analyze the flow response to externally applied fields with simple geometries (e.g., azimuthal, radial). Symmetry properties allow us to build selected induction modes whose interactions lead to dynamo mechanisms. Using an induction operator formalism, we show how dipole and quadrupole dynamos can be envisioned from such motions. The method identifies the main induction mechanisms that generate dynamo action in the selected geometry. Here, it emphasizes the competition between α-effect and field expulsion as well as the role of scale separation. © *2008 American Institute of Physics*. [DOI: 10.1063/1.2830983]

I. INTRODUCTION

The understanding of the self-sustained dynamo of the Earth is still a major challenge. Following Larmor's original hypothesis,[1] it is supposed to originate in the convective motion inside the liquid iron core. There, the induction due to fluid motions may overcome the Joule dissipation and a dynamo can be generated. Although knowledge of the fluid motion is essential because it drives the magnetic induction, the structure of the core convective motion is not precisely known. It is due to the extreme range of parameters in this problem: the Earth is in rapid rotation, and the electrical conductivity of molten iron is large, but finite. As a result, two important dimensionless parameters of the problem are very small: the Ekman number may be as low as 10^{-15} and magnetic Prandtl numbers of the order of 10^{-6},[2] are usually quoted. In addition, the source of the convective motion is mixed and still debated; thermal and compositional convection contribute, with heat and solute exchanged at the boundaries (solidification of the iron at the solid inner core, heat transfer at the mantle boundary) and heat is also possibly released in the core because of radioactive decay of ^{40}K.[3,4] The Rayleigh and Nusselt numbers are not precisely known, and the coupling with the magnetic field can result in significant changes in the structure of the convective flow. However, many models of the Earth's dynamo have invoked the columnar flow structure first derived by Busse[5] at the onset of convection in a spherical Couette geometry.[6] These columns may persist for a system moderately above the onset of convection[7,8] although their existence in the actual Earth's core is still an open question.[9] There are also arguments for a subcritical dynamo bifurcation,[10] in which the columnar structure may be stabilized by the large scale magnetic field.[11]

The focus of this paper is on the induction mechanisms that result from the existence of such a columnar structure. We consider a highly idealized situation in which columns with helical motion are distributed along a cylinder, as helicity is known to favor dynamo action.[12] The geometry is chosen to be cylindrical so that the curved boundary conditions of the Earth are ignored. We also do not take into account the drift of Busse's rolls, nor the presence of a zonal wind. The flow is prescribed, and we analyze its response to externally applied fields with simple geometries (azimuthal, radial, etc.) in order to understand the induction mechanisms in this system. For instance, several numerical simulations (e.g., Ref. 13, and references therein) have noticed that both dipole and quadrupole dynamos are possible, as well as coexisting modes with oscillatory instabilities, with thresholds in close proximity. These numerical studies focus on bifurcation diagrams. Our goal here is to detail how specific induction mechanisms interact to produce a dynamo cycle. The results emphasize the competition between α-effect and field expulsion, as they are observed in experiments, and on the action of scale separation on the expulsion effect.

Note that the periodic array of helical columns in the Roberts flow[14] and Karlsruhe dynamo[15] preferentially generates a transverse dipole. We show here that the annular geometry can lead to both axial dipoles and quadrupoles, as also shown in Ref. 16. We describe in detail the flow structure and the numerical method in Sec. II. In Sec. III we present our results concerning induction responses to simple applied fields. Section IV is devoted to the study of possible dynamo action in this type of flow, based on an operator formalism. Conclusions and possible extension of the study are presented in Sec. V.

II. SYSTEM AND METHODS

A. System

The flow geometry is made of a system of cylindrical columns forming an annulus, as shown in Fig. 1. The

columns are grouped in pairs of cyclonic and anticyclonic roll, for which the axial flow is reversed. The velocity is assumed to be stationary and is expressed as the sum of a contribution due to the circular motion of the fluid in a column [the *rotational* component $\mathbf{V}^R(\mathbf{r})$] and of a contribution due to an *axial* motion, which we label $\mathbf{V}^A(\mathbf{r})$. In an Earth-like geometry, $\mathbf{V}^A(\mathbf{r})$ would be generated by the Ekman pumping at the upper and lower boundaries. One thus writes

$$\mathbf{V}(\mathbf{r}) = \mathbf{V}^R(\mathbf{r}) + \xi \mathbf{V}^A(\mathbf{r}). \tag{1}$$

We chose analytical expressions of the fields such that the components are separately divergence-free, $\nabla \cdot \mathbf{V}^R(\mathbf{r}) = \nabla \cdot \mathbf{V}^A(\mathbf{r}) = 0$. The coefficient ξ measures the intensity of the axial motion compared to the rotational one.

The rotational part in columns of height $2H$ is expressed in cylindrical polar coordinates as

$$\mathbf{V}^R \begin{cases} V_r^R(r,\theta) = \sin(n\theta) \cdot \sin\left[\dfrac{\pi}{d}(r-(R-d))\right] \\ V_\theta^R(r,\theta) = \dfrac{1}{n}\cos(n\theta)\left\{\dfrac{\pi r}{d}\cos\left[\dfrac{\pi}{d}(r-(R-d))\right] + \sin\left[\dfrac{\pi}{d}(r-(R-d))\right]\right\} \\ V_z^R(r,\theta) = 0, \end{cases} \tag{2}$$

where n is the number of column pairs, R is the outer radius of the annulus, d is the thickness of the region in which the columns are confined (within radial distances between $R-d$ and R). The velocity is set to zero outside the domain $R-d \leqslant r \leqslant R$.

For the axial flow, we consider two cases. In the first one, the columns have a height $2H$ and the axial flow has a defined direction within each column and reverses between neighboring columns. It corresponds to the geometry sketched in Fig. 1(a). Figures 1(c) and 1(d) show, respectively, a cut of the flow in the planes $z=0$ and $\theta=0$. The helicity $[\mathcal{H}=\mathbf{V}\cdot(\nabla\times\mathbf{V})]$ has the same sign in each column, negative in this case (a column with positive axial velocity rotates with negative vorticity). The corresponding velocity is given by

$$\mathbf{V}^A \begin{cases} V_r^A(z,\theta) = 0 \\ V_\theta^A(z,\theta) = \dfrac{\pi r}{2nH}\sin(n\theta)\sin\left(\dfrac{\pi z}{2H}\right) \\ V_z^A(z,\theta) = \cos(n\theta)\cos\left(\dfrac{\pi z}{2H}\right). \end{cases} \tag{3}$$

In the second case [sketched in Fig. 1(b)], the axial flow is reversed about the plane $z=0$, hence having symmetries similar to Busse's columns in rotating convection. Figure 1(e) shows a cut of the flow in the plane $\theta=0$. The helicity is therefore negative in the columns of the upper half of the cylinder and positive in the lower half. The axial velocity is then written

$$\mathbf{V}^A \begin{cases} V_r^A(z,\theta) = 0 \\ V_\theta^A(z,\theta) = -\dfrac{\pi r}{nH}\sin(n\theta)\cos\left(\dfrac{\pi z}{H}\right) \\ V_z^A(z,\theta) = \cos(n\theta)\sin\left(\dfrac{\pi z}{H}\right). \end{cases} \tag{4}$$

In our study, we call $T1/2$ the configuration obtained with the rotational velocity and the first choice of the axial velocity field, and $T1$ the configuration obtained with the second choice. We shall look for stationary solutions of the induction equation,

$$\partial_t \mathbf{B} = 0 = \nabla \times (\mathbf{V} \times \mathbf{B}) + \eta \Delta \mathbf{B}, \tag{5}$$

where η is the magnetic diffusivity of the fluid. The boundary conditions are such that the medium inside the annulus has the same electrical conductivity as the fluid while the outside medium is insulating. The magnetic permeability is equal to that of vacuum in the whole space.

We stress that once the radius R of the cylinder and the aspect ratio $H/R=2$ are fixed there are still many independent parameters which may be varied: the number $2n$ of columns, their aspect ratio d/R, the magnitude of the axial flow compared to the rotational one, etc. We concentrate on the geometry portrayed in Fig. 1: four pairs of columns with relative thickness equal to 0.4 (yielding a square aspect ratio for the columns), and $\xi=1.25$ (this sets the ratio of the maxima of axial to rotational velocities to 0.7, close to the values in the existing experimental dynamos[15,17,18]). The only remaining free parameter is the amplitude of the velocity field, which is nondimensionalized in the form of the magnetic Reynolds number $R_m = V_{\max} R/\eta$. $V_{\max}$ is the maximum velocity in the domain of the flow, and we write $\mathbf{V} = V_{\max}\mathbf{v}$.

B. Iterative procedure

We use here the iterative technique introduced in Ref. 19. The reader is referred to it for a detailed presentation, and for an evaluation of its performance compared to standard analysis in magnetohydrodynamics. This type of self-consistent approach also underlies the method introduced by Stefani *et al.*[20] For low orders in the development, the method has been previously used for analytical studies,[21] including flows with a similar geometry as the one used here.[22]

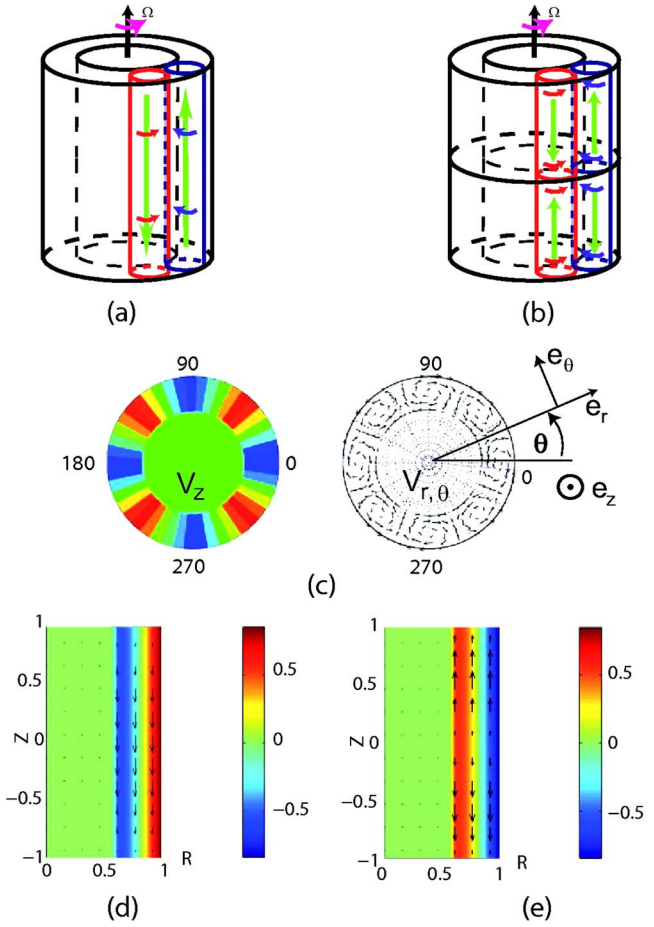

FIG. 1. (Color online) Geometry investigated. (a) Sketch of the column arrangement for the $T1/2$ flow. (b) Column arrangement for the $T1$ flow. (c) Cut of the $T1/2$ flow in the plane $z=0$ (shades correspond to the vertical flow, arrows correspond to the flow in the plane $z=0$). (d) Cut of the $T1/2$ flow in the plane $\theta=0$. (e) Cut of the $T1$ flow in the plane $\theta=0$.

We consider the response of the flow to an applied magnetic field $\mathbf{B}_0$, looking for the induced field $\mathbf{B}$ which solves the stationary induction equation

$$\nabla \times (\mathbf{V} \times \mathbf{B}) + \eta \Delta \mathbf{B} = -\nabla \times (\mathbf{V} \times \mathbf{B}_0). \tag{6}$$

The result is expressed as the integer series

$$\mathbf{B} = \sum_{k=1}^{\infty} \mathbf{B}_k \quad \text{with} \quad |\mathbf{B}_k| \sim \mathcal{O}(R_m^k) B_0. \tag{7}$$

The contributions $\mathbf{B}_k$ are computed iteratively from a hierarchy of nondimensional Poisson equations

$$\Delta \mathbf{B}_{k+1} = -R_m \nabla \times (\mathbf{v} \times \mathbf{B}_k), \quad k \geqslant 0, \tag{8}$$

which can be solved for any given set of boundary conditions.

C. Numerical simulation

Applying a standard Poisson solver to Eq. (8) would require us to write the complete set of conditions for the magnetic field at the boundaries of the computational domain. In practice, the boundary conditions are more readily expressed in terms of electric currents and potentials. We thus implement the following sequence:

(i) The electromotive force (emf in units of $V_{\max} B_0$) induced by the flow motion is computed from $\mathbf{e}_{k+1} = \mathbf{v} \times \mathbf{B}_k$.
(ii) Electric current being divergence free, the distribution of electric potential is obtained from $\Delta \phi_{k+1} = \nabla \cdot (\mathbf{v} \times \mathbf{B}_k)$, with von Neuman boundary conditions $[\mathbf{n} \cdot \nabla \phi = \mathbf{n} \cdot (\mathbf{v} \times \mathbf{B})$, with $\mathbf{n}$ the outgoing normal of the domain].
(iii) Induced currents (nondimensionalized) are then computed as from Ohm's law $\mathbf{j}_{k+1} = -\nabla \phi_{k+1} + \mathbf{e}_{k+1}$, and used to compute the magnetic field $\mathbf{B}_{k+1}$ from the Biot and Savart law.

All calculations are made with a magnetic Reynolds number equal to unity (we set $R=1$, $V_{\max}=1$ and $\eta=1$). Its actual value enters only in the final step, when contributions are collected and the integer series is computed, $\mathbf{B}(R_m) = \Sigma_k \mathbf{B}_k(R_m=1) R_m^k$. This approach requires that the series converges, and sets an upper value for the magnetic Reynolds number R_m $(R_m < R_m^*)$. We have found that the radius of convergence R_m^* is of the order of 30; for higher magnetic Reynolds number values we have shown in Ref. 19 that Padé approximants[23] still give results in remarkable agreement with the solution of the induction equation computed without approximation.

III. INDUCTION PROCESSES

In this section, we study how, at various stages of the iterative development, several magnetic modes can be obtained as the flow acts on externally applied fields with simple geometries. We will show in the next section how positive feedback loops can be constructed between combinations of the axisymmetric part of these modes. For this reason, as well as for the sake of simplicity, in the present section, the presentation of the induced fields and current densities is restricted to their axisymmetric part. This part is extracted by averaging any given quantity $\mathbf{A}(r,\theta,z)$ over the azimuthal angle θ,

$$\langle \mathbf{A} \rangle (r,z) \equiv \frac{1}{2\pi} \int_0^{2\pi} d\theta \mathbf{A}(r,\theta,z). \tag{9}$$

A. Induction from a toroidal applied field

When an external magnetic field is applied in the azimuthal direction ($\mathbf{B}_0 = B_0 \mathbf{e}_\theta$), one expects the generation of an azimuthal current, in very much the same manner as the α-effect[24] operates in the Roberts flow[14] and in the Karlsruhe dynamo.[15,25] This is because there is no conceptual difference between a horizontal field transverse to the columns in the Karlsruhe geometry and a toroidal field applied in the geometry considered here. In the azimuthal direction, there is a scale separation between the size of one column and the circumference of the annulus, so the results of mean-field MHD, as for instance explored in Ref. 26 should apply. Note

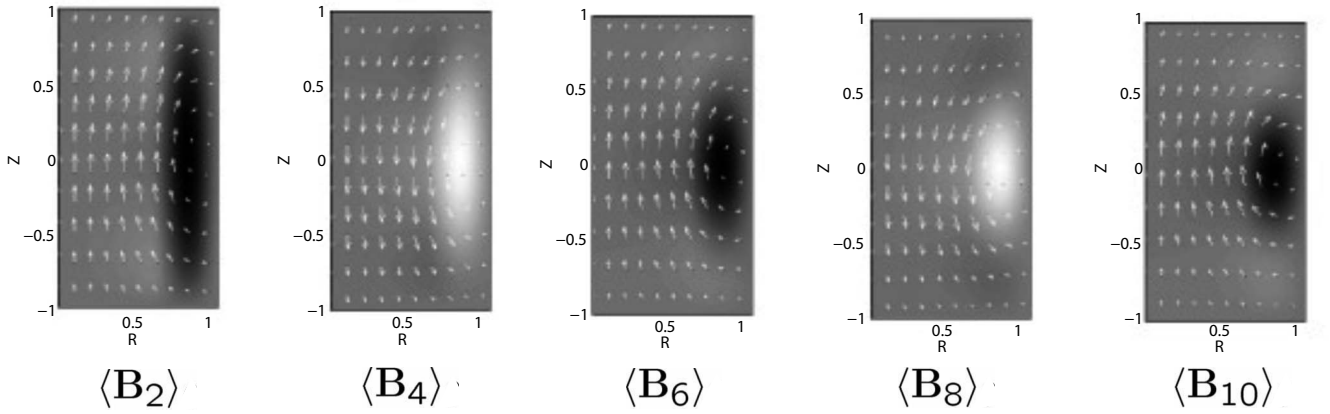

FIG. 2. $T1/2$: Applied toroidal field $B_{0,\theta}$. Structure of the azimuthal average $\langle \mathbf{B}_n \rangle$ of the fields induced at orders $n=2,4,6,8,10$.

that in the sequel, although our geometry is not spherical, we shall use the standard term "poloidal" to describe a magnetic field (or electrical current) with field lines in a meridian plane and the term "toroidal" will refer to fields with azimuthal field lines.

1. Basic mechanisms at first orders

The topology of $\mathbf{B}_0$ is chosen to be identical to the one that would be generated by the flow of an electric current in a rod of radius a located along the z-axis

$$\mathbf{B}_0 = B_0 \begin{cases} \dfrac{r}{a}\mathbf{e}_\theta & (r \leqslant a = 0.1), \\ \dfrac{a}{r}\mathbf{e}_\theta & (a \leqslant r). \end{cases} \tag{10}$$

The first order having a nonvanishing axisymmetric contribution is the second order. It is illustrated in the left panel of Fig. 2. The poloidal component (arrows) shows a dipolar structure, corresponding to an induced current parallel to the applied field $\mathbf{B}_0$ and having the symmetry of the flow helicity; as we have verified, this current is reversed as either $\mathbf{v}^A$ or $\mathbf{v}^R$ is reversed but not when both change sign. This type of effect, due to the helical motion in the columns, was first proposed by Parker,[27] and evidenced in the VKS experiment.[28] It is also in agreement with the α-effect introduced in the framework of mean-field magnetohydrodynamics,[24] for the 2D array of columns in the Roberts flow,[14] and for the columnar ring discussed here.[26] Following this analogy, we will call it α-effect in the rest of our study.

One can also observe on the left panel of Fig. 2 an induced toroidal field (gray scale), largest in the center of the columns and with its direction opposed to the applied field. This remains true even when the rotation of the columns is reversed, or when the axial flow is reversed or even suppressed. The effect traces back to the expulsion of magnetic field lines by vortical motions, as shown by numerical[29] and experimental[30] studies on an isolated vortex.

The response of the flow to an applied field is thus more complex than the generation of an azimuthal current $J_{2,\theta}$ by an α-effect due to the helical motion in the columns; this effect is indeed present, but the net current $\mathbf{J}_2$ is related to the applied field by a full second rank tensor, $\mathbf{J}_2 = \sigma[\alpha]\mathbf{B}_0$. In the tensor $[\alpha]$ not all components are due to the flow helicity and some components correspond to an expulsion effect.

2. Higher orders

As detailed in Ref. 19, the interest of the iterative procedure is to associate induction effects with specific actions of velocity gradients. It is particularly convenient when a patterns develops through the iterations. As it is the case here, we define a tool to help us quantify the convergence of the pattern. Let $\mathbf{B}_j$ and $\mathbf{B}_k$ be the fields induced at respective orders j and k. We compute the scalar product

$$(\mathbf{B}_j|\mathbf{B}_k) = \frac{1}{2\pi R^2 H}\int_V d^3 r \mathbf{B}_j \cdot \mathbf{B}_k, \tag{11}$$

and the associated norm $\mathcal{N}(\mathbf{B}_k) = \sqrt{(\mathbf{B}_k|\mathbf{B}_k)}$. Comparisons are made using the normalized scalar product

$$P_{j,k} = \left(\frac{\mathbf{B}_j}{\mathcal{N}(\mathbf{B}_j)} | \frac{\mathbf{B}_k}{\mathcal{N}(\mathbf{B}_k)} \right). \tag{12}$$

In the case of an azimuthal applied field, the expulsion eventually dominates. To wit, we compare in Fig. 2 successive iterations of the magnetic field $\langle \mathbf{B}_{2k} \rangle$. One finds $P_{2,4} \sim -0.95$, while $P_{2,3} < 10^{-3}$; the field induced at fourth order is almost exactly opposed to $\mathbf{B}_2$ and perpendicular to $\mathbf{B}_3$. As a result, the successive induction steps lead to the expulsion of the applied field, with $P_{k,k+1} \sim 0$ and $P_{k,k+2} \sim -1$, at higher orders. Bear in mind that this concerns normalized values. In dimensional units, one has

$$\mathbf{B}_{k+2} \sim \gamma \mathbf{B}_k, \quad \text{with } \gamma \sim -1/400. \tag{13}$$

After the tenth order, we could not detect any appreciable evolution of the pattern.

3. Evolution with R_m

The magnetic Reynolds number is reintroduced in the summation $\mathbf{B}_{\text{ind}} = \Sigma_{k=1}^{\infty} R_m^k \mathbf{B}_k$. We have summed terms up to order 22, resulting in a 1% accuracy. We show in Fig. 3 the evolution with R_m of two components of the induction: the

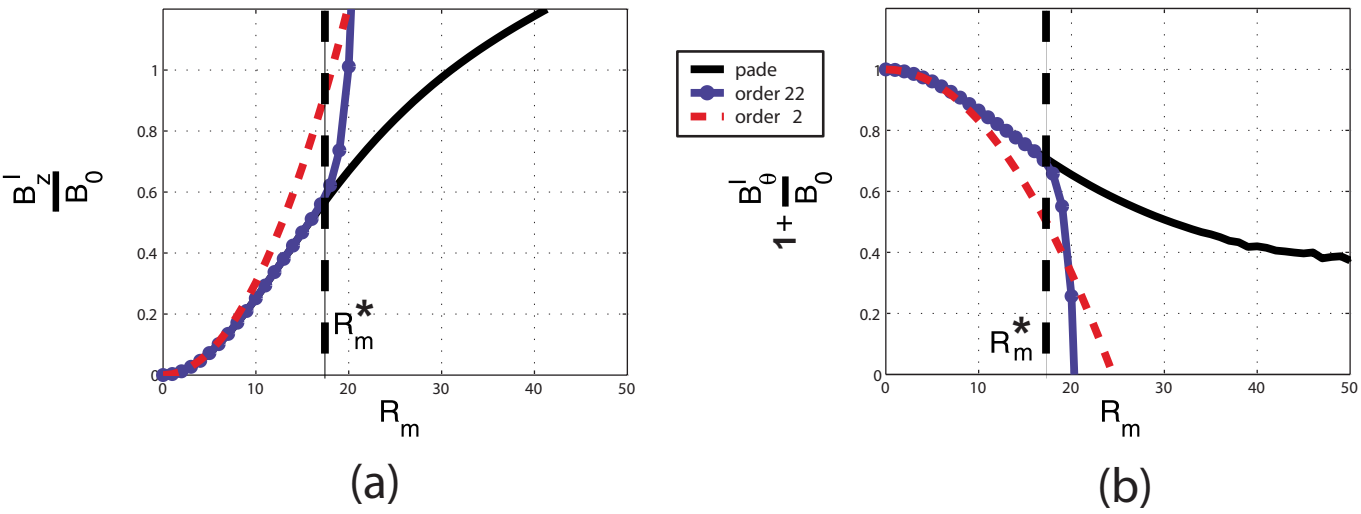

FIG. 3. (Color online) $T1/2$: evolution with R_m. (a) Axial field in the center of the annulus, at ($r=0$, $z=0$); (b) toroidal field in the columns, at ($r=0.8$, $z=0$). R_m^* is the radius of convergence of the integer series. The dashed line corresponds to the summation stopped at order 2, the continuous line with dots to the summation up to order 22, and the continuous line to the summation using Padé approximants.

axial field in the center of the cylinder, and the toroidal field in the center of the columns. For $R_m \leqslant 8$, the calculation at second order yields a very good approximation of the net induction. This is interesting because the second order truncation corresponds to the computation of the mean-field theory with a first order smoothing approximation.[26] For magnetic Reynolds numbers greater than about 8, the contributions of higher orders in the summation need to be taken into account. One finds that the mean-field approximation tends to overestimate the induced dipole field, Fig. 3(a), as well as the expulsion of the toroidal field, Fig. 3(b).

Empirically, we observe that the radius of convergence of the integer series is $R_m^*=17$. This value can be understood from our observation that $P_{k,k+1} \sim 0$ and $\mathbf{B}_{k+2} \sim \gamma \mathbf{B}_k$. Indeed one can then rewrite the summation as

$$\mathbf{B} = (\mathrm{R}_m \mathbf{B}_1 + R_m^2 \mathbf{B}_2) \sum_{k=0}^{\infty} (-|\gamma| R_m^2)^k, \tag{14}$$

from which one immediately gets $1/\sqrt{|\gamma|} \sim 20$ for the radius of convergence. In addition, for $R_m < R_m^*$, one gets

$$\mathbf{B} \simeq \frac{R_m}{1+|\gamma| R_m^2} \mathbf{B}_1 + \frac{R_m^2}{1+|\gamma| R_m^2} \mathbf{B}_2, \tag{15}$$

which shows that the divergence of the integer series actually lies in the existence of imaginary roots. Such a configuration is particularly suited to the use of Padé approximants.[23] The result, plotted as a solid line in Fig. 3, shows that at large magnetic Reynolds numbers ($R_m \geqslant 40$) the axial induction and the expulsion may saturate.

B. Induction from a radial field applied

As detailed above, starting from an applied toroidal field, the α-effect generates a poloidal induced field with a large axial component. But this axial component gives in turn very weak contributions to the induction; an applied field in the axial direction induces fields that are two orders of magnitude weaker than the values obtained with other orientations. In contrast, we show in this section that a radially applied field generates an induced field which has a significant component in the azimuthal direction.

Specifically, we consider an applied field $\mathbf{B}_0$ of the form

$$\mathbf{B}_0 = B_0 \begin{cases} \dfrac{r}{a} \mathbf{e}_r & (r \leqslant a = 0.1) \\ \dfrac{a}{r} \mathbf{e}_r & (a \leqslant r). \end{cases} \tag{16}$$

Two remarks about this functional form are in order:

(i) Within the domain of resolution of the induction equation it is essential that $\mathbf{B}_0$ be divergence free because we solve iteratively $\Delta \mathbf{B}_{k+1} = -\nabla \times (\mathbf{v} \times \mathbf{B}_k)$ rather than $\Delta \mathbf{B}_{k+1} = -\mathbf{v} \cdot \nabla \mathbf{B}_k - \mathbf{B}_k \cdot \nabla \mathbf{v}$.

(ii) Here, $\mathbf{B}_0$ is not divergence free for $r \leqslant a$, but in this domain the source term in $\Delta \mathbf{B}_1 = -\nabla \times (\mathbf{v} \times \mathbf{B}_0)$ vanishes with $\mathbf{v}$.

1. Basic mechanisms

For one individual column, a radial applied field is very similar to a toroidal applied field. Therefore, one expects the same mechanisms to be at play. The screw motion in the columns produces again a current parallel to the applied field. The current lines close inside the conducting fluid, leading to two poloidal loops. They generate a field $\langle \mathbf{B}_2 \rangle$ whose toroidal part is antisymmetric about the $z=0$ plane, as shown in Fig. 4 (left panel). The arrows in the same figure correspond to a poloidal field whose radial component is opposed to the applied field, as expected from an expulsion mechanism at play in the center of each column. In terms of amplitude, the radial/azimuthal conversion generated by the α-effect is of the same order of magnitude as the reverse process, discussed in the previous section. One computes $\max\{\langle B_{2,\theta} \rangle / B_{0,r}\} \sim 7 \cdot 10^{-4}$, to be compared to $\max\{\langle B_{2,r} \rangle / B_{0,\theta}\} \sim 11 \cdot 10^{-4}$ obtained in the case of the azimuthal applied field. However, the major difference is that

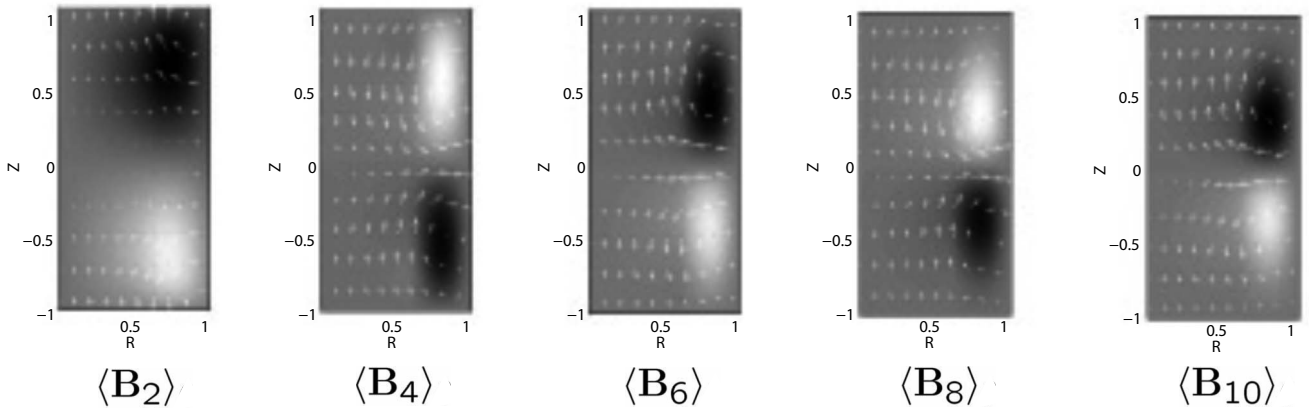

FIG. 4. $T1/2$: applied radial field $B_{0,r}$. Structure of the azimuthal average $\langle \mathbf{B}_n \rangle$ of the fields induced at orders $n=2,4,6,8,10$.

the expulsion is much weaker. The component of $\langle \mathbf{B}_2 \rangle$ opposed to the applied radial field is 10 times weaker than the induced toroidal field. This can be explained by the fact that, while $\mathbf{B}_2$ has a component opposed to the applied field in the center of the columns, it has a contribution which reinforces the applied field in their periphery. Therefore, when the azimuthal average is computed, the expulsion effect is weakened. On the contrary, in the case of the azimuthal applied field, the expulsion effects from each column was adding up collectively, resulting in a larger contribution.

Hence, expulsion is less effective in the direction perpendicular to the direction where scale separation develops (in the azimuthal direction the columns cross section is an order of magnitude smaller than the cylinder diameter, while in the radial direction the characteristic size of the flow is equal to the width of the column). We conclude that in the case considered here, scale separation does not particularly favor magnetic induction, but dramatically reduces expulsion.

2. Higher orders

The structure of the induced magnetic field is rapidly stabilized towards a quadrupolar structure as higher orders are computed. As shown in Fig. 4 the fields at all even orders closely resemble that at order 2, with a change of sign between consecutive even orders; the normalized scalar products are $P_{2,4} \sim -0.70$ and $P_{4,6} \sim -0.92$.

The fields produced at a given order are again fairly orthogonal to the fields at next or previous order: $(\mathbf{B}_k | \mathbf{B}_{k+1}) \sim 0$. In addition, as can be seen in Fig. 4, the iteration converges for even orders towards a quadrupolar structure with a negative feedback in a two step mechanism,

$$\mathbf{B}_{k+2} = -\gamma \mathbf{B}_k \ (\gamma \sim 1/415). \tag{17}$$

3. Evolution with R_m

The R_m dependence of the induced radial and azimuthal magnetic field is shown in Fig. 5, after summation of the

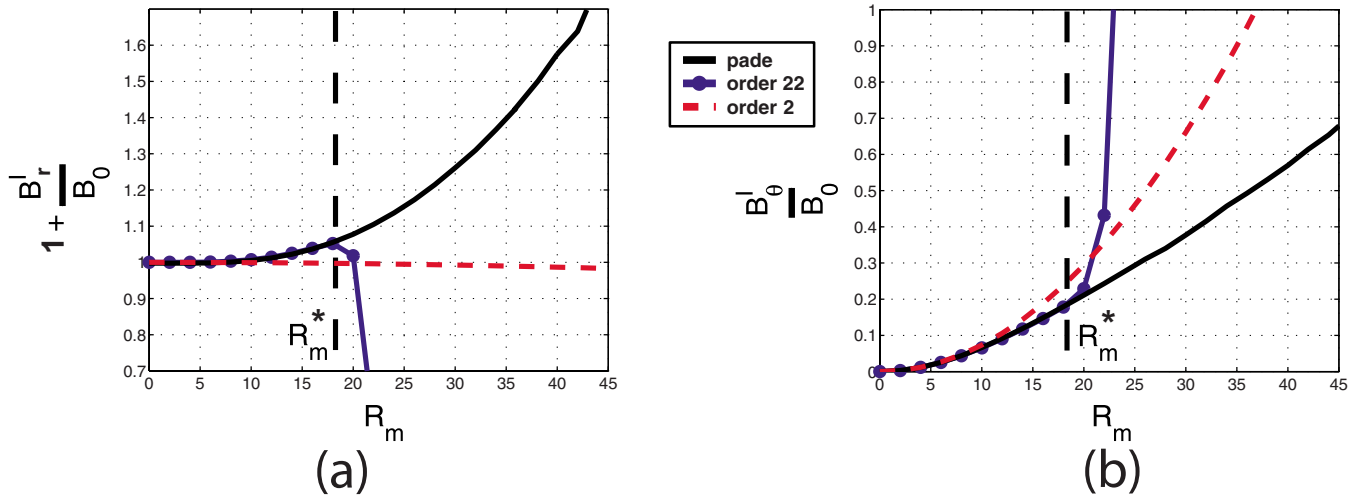

FIG. 5. (Color online) $T1/2$: induction at higher orders for an applied radial field $B_{0,r}$. Variation with R_m of the induced fields. (a) Radial induced component, sampled at $(r=0.7, z=0)$. (b) Azimuthal induced component, sampled at $(r=0.7, z=-0.6)$. The dashed line corresponds to the summation stopped at order 2, the continuous line with dots to the summation up to order 22, and the continuous line to the summation using Padé approximants.

terms up to order 22. Note that B_θ is sampled at $(r=0.7, z=-0.6)$, because for a quadrupole, the toroidal field is very weak in the $z=0$ plane. One observes in Fig. 5(b) that a second order calculation is a correct approximation for magnetic Reynolds numbers up to 10. For higher R_m other terms need to be included. As in the case of the toroidal applied field, they tend to slow the increase of the induced field, mainly because of expulsion generated from rotational motion in the columns. The integer series diverges for $R_m^*=18$, as expected from the value $1/\sqrt{|\gamma|}\sim 20$. Results obtained using Padé approximants, although extending the computed induction beyond the radius of convergence of the series, do not point to a saturation at large R_m.

IV. DYNAMO ACTION

In the previous section, we showed that the induction mechanisms in the case of the $T1/2$ flow consist of a mutual conversion between azimuthal and radial fields, through the α-effect, along with an effect of expulsion of these fields by the rotating columns. We have identified two modes, dipole and quadrupole, mainly axisymmetric, that realize a feedback loop in a two-step mechanism [Eqs. (13) and (17)] with a negative sign, therefore leading to an antidynamo configuration. Following the ideas developed in Ref. 19, we can express these results using an induction operator formalism. From Eq. (8), we define $\mathcal{L}(R_m)\equiv -R_m\Delta^{-1}\{\nabla\times(\mathbf{v}\times\cdot)\}$ for a velocity field $\mathbf{v}$ corresponding to the value $R_m=1$. Equations (13) and (17) can then be interpreted in the following way: the $\langle\mathbf{B}_{2n}\rangle$ modes $(n>5)$ obtained in the induction studies in Secs. III A (dipole mode) and III B (quadrupole mode) are eigenvectors of $\mathcal{L}^2(R_m)$. From this observation, we will show in this section that using a poloidal/toroidal decomposition, a matrix analysis can be performed on the identified eigenmodes to find eigenvectors of $\mathcal{L}^2(R_m)$ with positive eigenvalues, thus leading to possible dynamo solutions. Writing for simplicity $\mathcal{L}=\mathcal{L}(1)$ [we then have $\mathcal{L}(R_m)\mathbf{B}=R_m\mathcal{L}\mathbf{B}$], let us assume that we can find a magnetic field $\mathbf{B}_e$ that is not an eigenvector of the operator $\mathcal{L}$, but of $\mathcal{L}^2$ with a positive eigenvalue γ_e; then, $\mathbf{B}_s=\mathbf{B}_e+1/\sqrt{\gamma_e}\mathcal{L}\mathbf{B}_e$ is an eigenvector of $\mathcal{L}$ with a positive eigenvalue $\gamma_s=\sqrt{\gamma_e}$. Taking $R_m=1/\sqrt{\gamma_e}$, we then have $\mathcal{L}(R_m)\mathbf{B}_s=\mathbf{B}_s$, which defines $\mathbf{B}_s$ as a self-sustained magnetic field in the corresponding velocity field, at threshold $R_m=1/\sqrt{\gamma_e}$.

We emphasize that this method is more complex than an eigenvalue calculation. In addition, as will become clearer later, it does not strictly respect the symmetries,[16] since approximations have to be made when projecting the results of the application of the operator $\mathcal{L}^2$ onto the initial vectors. We will discuss the validity of all approximations and show that the technique helps understanding not only the dynamo modes and their thresholds but also how the induction effects can combine to produce a dynamo.

A. Dynamo action in the *T1/2* flow

We first illustrate our method with an example: the generation of a dipole field for a given flow. We use this example to estimate the error associated to the approximations made in the method.

1. Method and error estimates: Example of the generation of a dipole field

We start from the field $\langle\mathbf{B}_{10}\rangle$ (Fig. 2), which was shown [Eq. (13)] to be an eigenvector of $\mathcal{L}^2$, with a dipolar geometry and a negative eigenvalue. Since a dynamo cycle is often seen as a toroidal/poloidal feedback loop,[12] we decompose this field into its toroidal—$\mathbf{B}_d^T$—and poloidal—$\mathbf{B}_d^P$—components, to which we apply the operator $\mathcal{L}^2$. As expected, the resulting fields are of opposite sign with respect to $\mathbf{B}_d^T$ and $\mathbf{B}_d^P$. In addition, their topology are very similar and look like a linear combination of the initial fields $\mathbf{B}_d^T$ and $\mathbf{B}_d^P$. Using the scalar products defined in Eq. (11), we can project $\langle\mathcal{L}^2\mathbf{B}_d^T\rangle$ and $\langle\mathcal{L}^2\mathbf{B}_d^P\rangle$ onto the initial fields, thus defining an induction matrix,

$$M_d(T1/2)=\begin{pmatrix} M_{PP} & M_{PT} \\ M_{TP} & M_{TT}\end{pmatrix} = \begin{pmatrix} (\langle\mathcal{L}^2B_d^P\rangle|B_d^P) & (\langle\mathcal{L}^2B_d^P\rangle|B_d^T) \\ (\langle\mathcal{L}^2B_d^T\rangle|B_d^P) & (\langle\mathcal{L}^2B_d^T\rangle|B_d^T)\end{pmatrix}, \tag{18}$$

where we have taken $\mathcal{N}(\mathbf{B}_d^T)=\mathcal{N}(\mathbf{B}_d^P)=1$, using the norm $\mathcal{N}$ defined in Sec. III A 2. This matrix $M_d(T1/2)$ is the restriction of the two-step induction operator $\mathcal{L}^2$ to the vector space of the axisymmetric dipoles. The diagonal terms represent the expulsion effect and the extra-diagonal terms represent the action of the α-effect. Positive eigenvalues correspond to an axisymmetric dipolar dynamo.

Let us discuss the approximations made in this method. We have assumed so far that $\langle\mathcal{L}^2\mathbf{B}_d^T\rangle$ and $\langle\mathcal{L}^2\mathbf{B}_d^P\rangle$ belong to the vector space generated by $\mathbf{B}_d^T$ and $\mathbf{B}_d^P$. In order to check the validity of this hypothesis, we show some comparisons in Fig. 6, using profiles normalized by their maximum value: in (a) the axial profiles of the radial component of $\langle\mathcal{L}^2\mathbf{B}_d^T\rangle$ and $\langle\mathcal{L}^2\mathbf{B}_d^P\rangle$ are compared to the equivalent profile for $\mathbf{B}_d^P$. One can see that the overlap is very good. In (b), the radial profiles of the azimuthal component of $\langle\mathcal{L}^2\mathbf{B}_d^T\rangle$ and $\langle\mathcal{L}^2\mathbf{B}_d^P\rangle$ are compared to the radial profile for $\mathbf{B}_d^T$. In the case of the α-effect ($\langle\mathcal{L}^2\mathbf{B}_d^P\rangle$ profile), the overlap is very good again. In the case of the expulsion effect ($\langle\mathcal{L}^2\mathbf{B}_d^T\rangle$ profile), there is a discrepancy. We have computed the error to be about 10%. Thus the M_{TT} term in the matrix represents the expulsion mechanism for the applied toroidal field within an error of 10%, while the other elements of the matrix can be considered as correct within less than 1%.

2. General expression for the matrix M

By redefining the $\mathcal{L}$ operator as a linear function of the poloidal and toroidal components of the flow, we obtain a general expression of the matrix M, for any value of the axial/rotational ratio (ξ parameter). We normalize the components $\mathbf{v}^A$ and $\mathbf{v}^R$ of the velocity field, $\max(\mathbf{v}^A)=1$ and $\max(\mathbf{v}^R)=1$ and rewrite Eq. (1) as $\mathbf{V}=V_A\mathbf{v}^A+V_R\mathbf{v}^R$, where V_A and V_R represent the maximum amplitude of each component. Let $\mathcal{L}_A$ be the induction operator when $\mathbf{V}=\mathbf{v}^A$ and $\mathcal{L}_R$ be the induction operator when $\mathbf{V}=\mathbf{v}^R$; $\mathcal{L}$ can then be written as the linear combination,

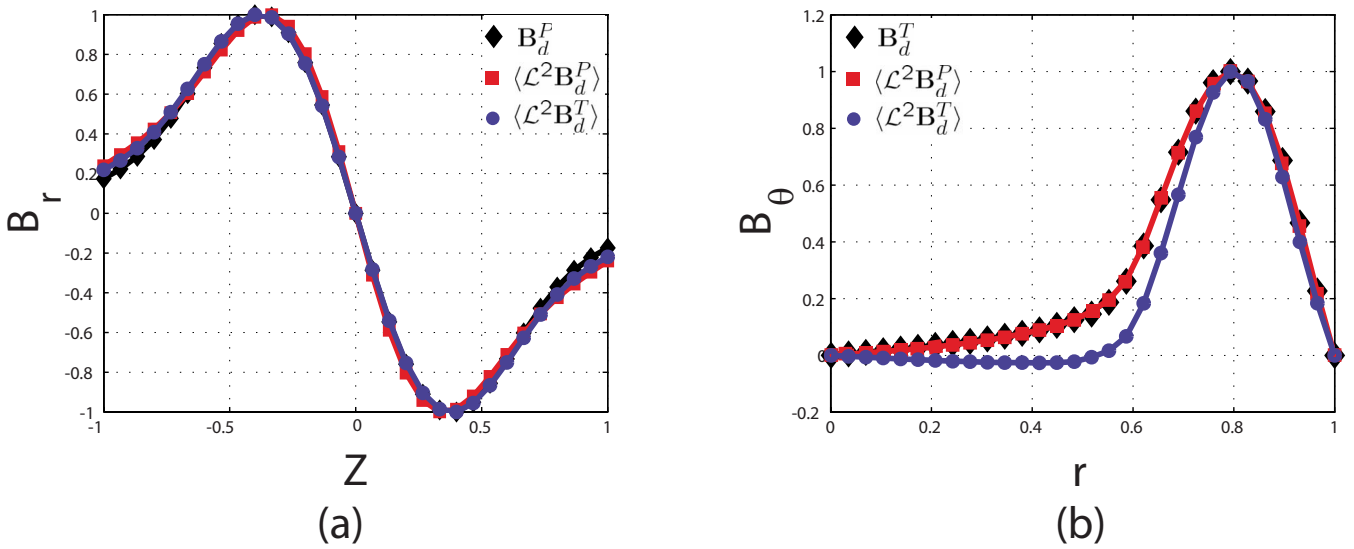

FIG. 6. (Color online) Dipolar mode: estimate of the error made doing the projection (a) axial profile of B_r at $r=0.8$ from the Oz axis. (b) Radial profile of B_θ in the median plane. (■): Components of the applied field. (♦): Components of $\langle \mathcal{L}^2 \mathbf{B}_d^P \rangle$. (●): Components of $\langle \mathcal{L}^2 \mathbf{B}_d^T \rangle$.

$$\mathcal{L} = V_A \mathcal{L}_A + V_R \mathcal{L}_R, \tag{19}$$

yielding

$$\mathcal{L}^2 = V_A^2 \mathcal{L}_A \mathcal{L}_A + V_A V_R (\mathcal{L}_R \mathcal{L}_A + \mathcal{L}_A \mathcal{L}_R) + V_R^2 \mathcal{L}_R \mathcal{L}_R, \tag{20}$$

so that the four matrix elements M_{ij} can also be written as quadratic forms of V_A and V_R,

$$M_{ij} = a_{ij} V_A^2 + b_{ij} V_R V_A + c_{ij} V_R^2. \tag{21}$$

As we studied the induction mechanisms, we noticed that the α-effect and the expulsion behave differently under a reversal of the axial pumping ($V_A \to -V_A$) or of the columns rotation ($V_R \to -V_R$). More precisely, it was observed that the expulsion effect is independent of these sign changes, whereas the α-effect transforms as the product $V_A V_R$. These observations allow to eliminate some terms in Eq. (21), yielding

$$M(V_R, V_A) = \begin{pmatrix} aV_R^2 + bV_A^2 & cV_R V_A \\ dV_R V_A & eV_R^2 + fV_A^2 \end{pmatrix}. \tag{22}$$

We will now compute the value of these six coefficients in the case of the $T1/2$ flow. The corresponding expressions for the matrix M are the following:

Axial dipole:

We use here the axial dipole basis, defined in Sec. IV A 1,

$$M_d(V_A, V_R) = -10^{-4} \begin{pmatrix} 22V_A^2 + 6V_R^2 & 46V_A V_R \\ 18V_A V_R & 14(V_A^2 + V_R^2) \end{pmatrix}. \tag{23}$$

Axial quadrupole:

In this case, the generating vectors are formed by the poloidal and toroidal components of the field $\langle B_{10} \rangle$ presented in Fig. 4, which was shown [Eq. (17)] to be an eigenvector of the operator $\mathcal{L}^2$, with a quadrupolar geometry and a negative eigenvalue. This mode is orthogonal to the dipole mode,

$$M_q(V_A, V_R) = -10^{-4} \begin{pmatrix} 23V_A^2 + 5V_R^2 & 25V_A V_R \\ 25V_A V_R & 11(V_A^2 + V_R^2) \end{pmatrix}. \tag{24}$$

Transverse dipole:

Until now, we have only considered axisymmetric fields. However, since the $T1/2$ flow presents several analogies with the Roberts flow, it would be interesting to study the possibility of generating a transverse dipole (perpendicular to the columns), as observed in the Karlsruhe dynamo.[15] We follow the same strategy as before: a uniform transverse field $\mathbf{B}_0 = B_0 \mathbf{e}_x$ (where the direction of $\mathbf{e}_x$ is given by $\theta=0$, see Fig. 1) is applied to the flow and we compute the fields $\mathbf{B}_k$ obtained after k iterations. They rapidly converge towards a stable structure. After 8 iterations, the fields $\mathbf{B}_k$ and $\mathcal{L}^2 \mathbf{B}_k$ have an overlap close to 100%, and the eigenvalue is negative, $\gamma = -1/400$. This nonaxisymmetric mode cannot be decomposed into a poloidal and toroidal part but we noticed previously that this decomposition also separated symmetric and antisymmetric components, under the reflection symmetry with respect to the plane $z=0$. In the same way, the mode $\mathbf{B}_8$ obtained here can be decomposed into its symmetric and antisymmetric parts, that form a generating basis. Using this basis, the matrix M is

$$M_t(V_A, V_R) = -10^{-4} \begin{pmatrix} 22V_A^2 + 13V_R^2 & 29V_A V_R \\ 46V_A V_R & 16V_A^2 + 14V_R^2 \end{pmatrix}. \tag{25}$$

3. Dynamo capability of T1/2 flow

From the expressions of the matrix M obtained in the previous paragraph, the largest eigenvalue $\lambda_{\max}$ of each matrix can be computed as a function of V_A and V_R. The result is shown in Fig. 7. In order to facilitate the reading of these plots, when $\lambda_{\max}$ was negative (no dynamo), we artificially set its value to zero. For each case, two regions are evidenced: the first one, for which $\lambda_{\max} > 0$, corresponds to the possibility to observe a dynamo for the considered

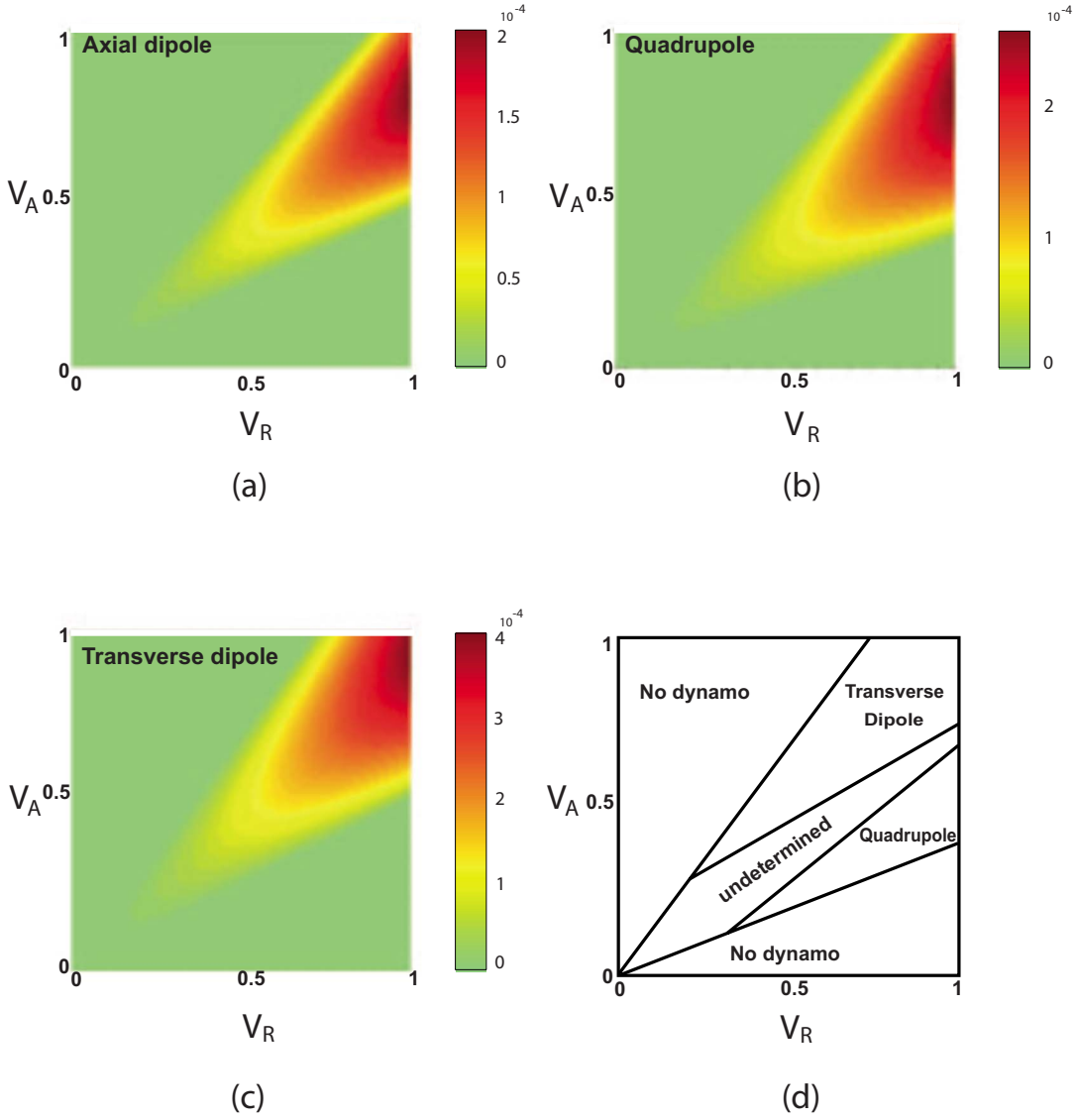

FIG. 7. (Color online) $T1/2$ flow: evolution of the largest eigenvalue of the induction matrix in the (V_R, V_A) plane. (a) Axial dipole; (b) axial quadrupole; (c) transverse dipole; (d) predominance diagram for the different possible modes. For simplicity, when the eigenvalue is negative we plotted a zero value.

geometric parameters ($d/r=0.4$ and $n=4$) with a threshold $R_m^c=1/\sqrt{\lambda_{\max}}$. The second, for which $\lambda_{\max}<0$, corresponds to the case where no dynamo instability can take place. Figures 7(a)–7(c) show that the three dynamo modes coexist in the same region, in the neighborhood of the line $V_A=V_R$. This is not surprising, since when one of the velocity component dominates the other, the expulsion mechanism is more important than the α-effect, which needs both components together.

For a given couple (V_A, V_R), one can observe that λ_q is always larger than λ_d (corresponding to a lower threshold). In the same way, the transverse dipole always has a lower threshold than the axial dipole. A summary of the predominance of the different modes is given in Fig. 7(d), where one can see that the transverse dipole is favored by higher ratio axial/rotational, whereas the quadrupole is favored by a lower ratio.

The case of the transverse dipole mode is interesting, since it sheds light on the Karlsruhe dynamo, using the analogies between the $T1/2$ flow and the Roberts flow. As suggested earlier in Refs. 31 and 32, along the two directions perpendicular to the pipes, the two components of the field transform into one another through an α-effect.

In a $T1/2$ flow, we thus observed that several dynamo modes can be sustained when $R_m \simeq 80$. This result is consistent with other numerical studies in thermal convection,[33] which have shown that various dynamo solutions can coexist in the same region of the parameter space. This kind of behavior has also been observed in the VKS dynamo experiment,[34] where different dynamo modes (steady, chaotically reversing, bursts, periodic) can be obtained when changing the rotation rate of the driving impellers.

B. Dynamo mechanisms in the *T*1 flow

The analytical expression of the $T1$ flow is given in Eq. (4). Compared to the $T1/2$ flow [Eq. (3)], the only difference is that the azimuthal and axial components are now, respec-

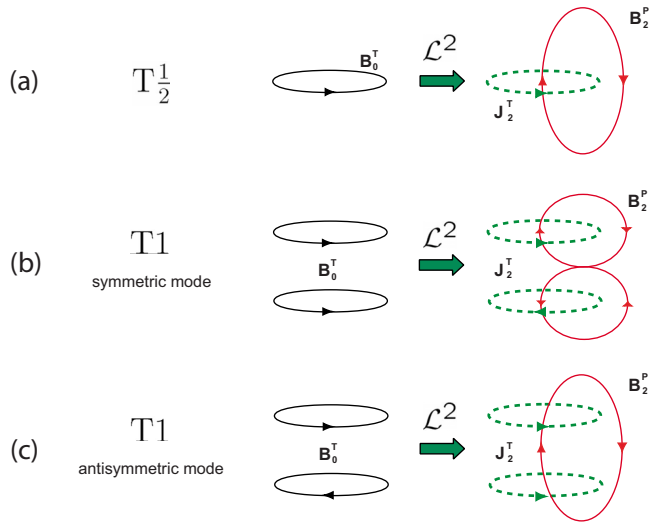

FIG. 8. (Color online) Comparison between the schematic induction mechanisms for the $T1/2$ and $T1$ flows, due to the α-effect in the case of a toroidal applied field. The lines in the second column represents the applied field, and in the third column, the dashed line represents the resulting order 2 current and the solid line the resulting order 2 magnetic field. (a) $T1/2$ flow; (b) $T1$ flow, with a symmetric applied field; (c) $T1$ flow, with an antisymmetric applied field.

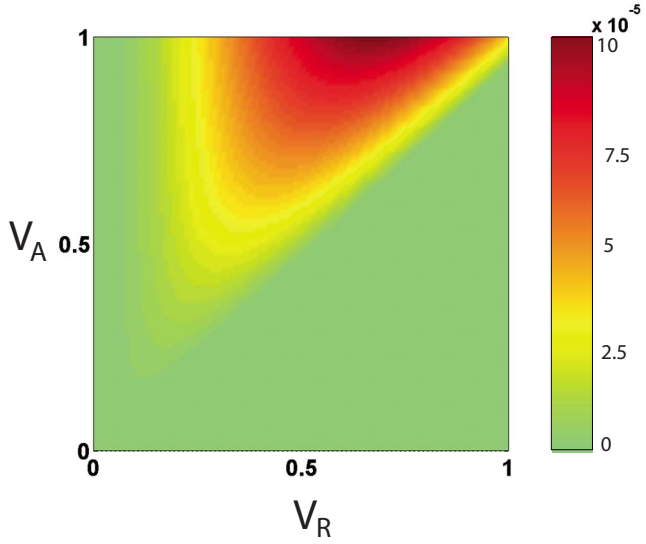

FIG. 9. (Color online) $T1$ flow: evolution of the largest eigenvalue of the induction matrix in the (V_R, V_A) plane, for the axial quadrupole. For simplicity, when the eigenvalue is negative we plotted a zero value.

tively, symmetric and antisymmetric under $\mathcal{S}_z$. $T1$ is a superposition of two $T1/2$ flows, one in each half-cylinder, symmetric with respect to $\mathcal{S}_z$. They have opposite helicity, since their axial component is reversed, while the rotation of the columns is unchanged. The strong similarity between the $T1/2$ and $T1$ flows indicates that the same mechanisms, α-effect and expulsion, will take place. Figure 8 compares the schematic induction mechanisms for the α-effect in both types of flow. In (a), the case of the $T1/2$ flow is recalled, where the induced current ($\mathbf{j}=\sigma\alpha\mathbf{B}$) is parallel to the applied field with the same sign, since helicity $\mathcal{H}$ is negative in this flow and the α coefficient is proportional to $-\mathcal{H}$. In (b), it is shown that in the $T1$ flow, applying a symmetric toroidal field results in a symmetric poloidal field, corresponding to a quadrupolar geometry. In (c), we show that the dipolar geometry (antisymmetric poloidal field) is obtained by applying an antisymmetric toroidal field.

Based on these symmetry considerations, the dipolar mode for the $T1$ flow was built by applying $\mathcal{L}$ iteratively to an initial toroidal field antisymmetric with respect to $\mathcal{S}_z$. We chose an initial field of the form $\mathbf{B}_0=B_0 \sin(\pi z/H)\mathbf{e}_\theta$. The iterations converge rapidly towards a mode whose toroidal and poloidal parts, once the azimuthal average is done, form a basis which is closed under the action of $\mathcal{L}^2$. In the same way, the quadrupolar generating basis was constructed starting from an azimuthal z-independent field [note that an identical mode is obtained if one starts from a symmetric radial field of the form $\mathbf{B}_0=B_0 a/r \cos(\pi z/H)\mathbf{e}_r$].

As for the transverse mode, we tried to follow the same procedure used in the case of the $T1/2$ flow, but it turned out that the converged mode, starting from an initial uniform transverse field, is formed of two dipolar structures at 90° from each other, having the same behavior under the reflection symmetry with respect to the plane $z=0$. Therefore, it is not possible to use this symmetry to construct the basis vectors. And we were indeed unable to find any basis that would be closed under the action of $\mathcal{L}^2$. This shows a limitation of our method.

The expressions for the matrix M obtained are:

Dipolar mode:

$$M_d(V_A,V_R) = -10^{-4}\begin{pmatrix} 16V_A^2+8V_R^2 & 33V_AV_R \\ 16V_AV_R & 12(V_A^2+V_R^2) \end{pmatrix}. \quad (26)$$

There is no value of the couple (V_A, V_R) for which the axial dipole can be sustained by the $T1$ flow. Some studies have shown[35] that in order for a $T1$-type flow to sustain an axial dipole, the presence of differential rotation, absent in our study, would be necessary.

Axial quadrupole:

$$M_q(V_A,V_R) = -10^{-4}\begin{pmatrix} 20V_A^2+5V_R^2 & 25V_AV_R \\ 20V_AV_R & 11V_A^2+8V_R^2 \end{pmatrix}. \quad (27)$$

Figure 9 shows the evolution of $\lambda_{\max}$ in the case of the quadrupole mode. It is interesting to note that in all the cases where a dynamo was possible, the corresponding matrix $[M_d(T1/2), M_q(T1/2), M_t(T1/2)$, and $M_q(T1)]$ presented the following characteristics: one could find values of the couple (V_A, V_R) so that the product of the nondiagonal terms was larger than the product of the diagonal terms. One can easily show that this is a necessary and sufficient condition for a 2×2 matrix (with negative diagonal coefficients) to have a positive eigenvalue. And this condition physically corresponds to the facts that the expulsion mechanism (diagonal terms) is weaker than the α mechanism (nondiagonal terms). On the contrary, in the case of $[M_d(T1)]$, this condition is not met.

V. CONCLUDING REMARKS

A better understanding of the MHD induction mechanisms in a given system can help to build dynamo cycles. In

the first part of this study, we have identified two mechanisms, related, respectively, to the α-effect and to expulsion by vortices. We expressed these mechanisms in terms of the induction operator $\mathcal{L}^2$ and, using a poloidal/toroidal decomposition of the eigenvectors of $\mathcal{L}^2$, we were able to perform a matrix analysis leading to the determination of self-sustained magnetic modes. This analysis not only allows to predict a threshold for these dynamo modes, as could indeed have been computed using more standard eigenvalue computation, but the additional benefit is that it also brings a new insight into these modes, providing the actual induction mechanisms which combine to produce a dynamo effect. In regards to natural or experimental conditions, it helps understand which features of the velocity field favor or hinder dynamo action. In addition, as already noticed in other studies,[36] the competition between the α-effect, favorable to the dynamo, and the expulsion effect, that works against it, can be monitored by the ratio of poloidal to toroidal components of the velocity field (in our case the axial to rotational ratio V_A/V_R). Our studies show that a positive feedback requires a comparable amplitude for rotation and pumping. In the case of the $T1/2$ flow (for eight columns and an aspect ratio of 0.4), we observed that both axisymmetric modes (dipolar and quadrupolar) can be sustained, with a threshold of the order of $R_m = 100$. We also showed that a transverse dipole mode can exist, as one could expect, because of the analogy between our flow and the Karlsruhe dynamo. On the other hand, the $T1$ flow can only sustain a quadrupolar mode, when the pumping amplitude is larger than the rotation amplitude. For the axial dipole mode, the poloidal to toroidal conversion seems too weak to compensate for the strong expulsion of the azimuthal field.

This study also provides a better understanding of the role of scale separation; it does not particularly enhance the induction effects, but rather reduces the field expulsion in the direction perpendicular to the separation, thus indirectly favoring the dynamo process.

Coming back to the Earth's case, our model system leads to several observations. An α^2 dynamo process relies on the helicity contained in Busse's columns,[5] but Ekman pumping would give a very weak source of axial motion, since the Ekman number E is of the order of 10^{-15} and the ratio of the axial flow to the rotational flow scales like $E^{1/2}$.[37] Another source of axial velocity could be the β-effect due to the curvature of the core-mantle boundary—note that in this case the axial flow is in phase with the radial flow rather than with the vorticity.[35] A large scale dipole field could also be generated from an $\alpha-\omega$ dynamo. It would require differential rotation as provided, for instance, by zonal winds[38,39] or super-rotation effects as observed in the DTS laboratory experiment.[40] These ingredients could in principle be added to the model studied here, and the procedure used to determine which dynamo modes (dipole, quadrupole or other) are likely to exist for a given range of Reynolds numbers. As proposed for geomagnetism,[41] and recently observed in the VKS experiment,[34] the close proximity of dynamo modes may be essential for the development of dynamical regimes.

ACKNOWLEDGMENTS

We acknowledge useful discussions with M. Bourgoin, R. Avalos-Zuñiga, P. Cardin, F. Plunian, and N. Schaeffer. This work was partially supported by the Émergence Program of the Rhône-Alpes Region (France).

[1] J. Larmor, "How could a rotating body such as the sun become a magnet?" Report of the 87th meeting of the British Association for the Advancement of Science (1919), pp. 159–160.
[2] J.-P. Poirier, "Physical properties of the Earth core," C. R. Seances Acad. Sci. II **318**, 341 (1994).
[3] S. Labrosse, "Thermal and magnetic evolution of the Earth core," Phys. Earth Planet. Inter. **140**, 127 (2003).
[4] S. L. Butler, W. R. Peltier, and S. O. Costin, "Numerical models of the Earth's thermal history: Effects of inner-core solidification and core potassium," Phys. Earth Planet. Inter. **152**, 22 (2005).
[5] F. H. Busse, "Thermal instabilities in rapidly rotating systems," J. Fluid Mech. **44**, 441 (1970); C. R. Carrigan and F. H. Busse, "An experimental investigation of the onset of convection in rotating spherical shells," *ibid.* **126**, 287 (1983).
[6] U. R. Christensen, J. Aubert, P. Cardin, E. Dormy, S. Gibbons, G. A. Glatzmaier, E. Grote, Y. Honkura, C. Jones, M. Kono, M. Matsushima, A. Sakuraba, F. Takahashi, A. Tilgner, J. Wicht, and K. Zhang, "A numerical dynamo benchmark," Phys. Earth Planet. Inter. **128**, 25 (2001); E. Dormy, A. M. Soward, C. A. Jones, D. Jault, and P. Cardin, "The onset of thermal convection in rotating spherical shells," J. Fluid Mech. **501**, 43 (2004).
[7] E. Dormy, J.-P. Valet, and V. Courtillot, "Numerical models of the geodynamo and observational constraints," Geochem., Geophys., Geosyst. **1**, 62 (2000).
[8] V. Morin and E. Dormy, "Dissipation mechanisms for convection in rapidly rotating spheres and the formation of banded structures," Phys. Fluids **18**, 068104 (2006).
[9] H. Harder and U. Hansen, "A finite volume solution method for the thermal convection and dynamo problem is spherical shells," Geophys. J. Int. **161**, 522, DOI: 10.1111/j.1365-246X.2005.02560.x (2005).
[10] V. Morin, Ph.D. thesis, Université Denis Diderot-Paris (2005).
[11] F. H. Busse, "Convective flows in rapidly rotating spheres and their dynamo action," Phys. Fluids **14**, 1301 (2002).
[12] H. K. Moffatt, *Magnetic Field Generation in Electrically Conducting Fluids* (Cambridge University Press, Cambridge, 1978).
[13] E. Grote, F. H. Busse, and A. Tilgner, "Convection-driven quadrupolar dynamos in rotating spherical shells," Phys. Rev. E **60**, R5025 (1999).
[14] G. O. Roberts, "Dynamo action of fluid motions with two-dimensional periodicity," Philos. Trans. R. Soc. London, Ser. A **271**, 41 (1972).
[15] R. Stieglitz and U. Müller, "Experimental demonstration of a homogeneous two-scale dynamo," Phys. Fluids **13**, 561 (2001).
[16] A. Tilgner, "Small scale kinematic dynamos: beyond the α-effect," Geophys. Astrophys. Fluid Dyn. **98**, 225, DOI: 10.1080/0309192042000196103 (2004).
[17] A. Gailitis, O. Lielausis, S. Dement'ev, E. Platacis, and A. Cifersons, "Detection of a flow induced magnetic field eigenmode in the Riga dynamo facility," Phys. Rev. Lett. **84**, 4365 (2000).
[18] R. Monchaux, M. Berhanu, M. Bourgoin, M. Moulin, Ph. Odier, J.-F. Pinton, R. Volk, S. Fauve, N. Mordant, F. Pétrélis, A. Chiffaudel, F. Daviaud, B. Dubrulle, C. Gasquet, L. Marié, and F. Ravelet, "Generation of magnetic field by dynamo action in a turbulent flow of liquid sodium," Phys. Rev. Lett. **98**, 044502 (2007).
[19] M. Bourgoin, P. Odier, J.-F. Pinton, and Y. Ricard, "An iterative study of time independent induction effects in magnetohydrodynamics," Phys. Fluids **16**, 2529 (2004).
[20] See also F. Stefani, G. Gerbeth, and K. H. Rädler, "Steady dynamos in finite domains: An integral equation approach," Astron. Nachr. **321**, 65 (2000).
[21] K.-H. Rädler, M. Rheinhardt, E. Apstein, and H. Fuchs, "On the mean-field theory of the Karlsruhe dynamo experiment," Nonlinear Processes Geophys. **9**, 171 (2002).
[22] F. H. Busse, "A model of the geodynamo," Geophys. J. **42**, 437 (1975).
[23] W. H. Press, S. A. Teukolsky, W. T. Vetterling, and B. P. Flannery, *Numerical Recipes* (Cambridge University Press, Cambridge, 1986).

[24]F. Krause and K.-H. Rädler, *Mean Field Magnetohydrodynamics and Dynamo Theory* (Pergamon, New York, 1980).
[25]A. Tilgner, "A kinematic dynamo with a small scale velocity field," Phys. Lett. A **226**, 75 (1997).
[26]R. A. Avalos-Zuñiga, F. Plunian, and K. H. Rädler, "Mean electromotive force generated by a ring of helical vortices," in *Proceedings of the 21st ICTAM*, 15–21 August 2004, Warsaw, Poland, edited by W. Gutkowski and T. A. Kowaleski (Springer, Dordrecht, The Netherlands, 2005).
[27]E. N. Parker, "Hydromagnetic dynamo models," Astrophys. J. **122**, 293 (1955).
[28]F. Pétrélis, M. Bourgoin, L. Marié, J. Burguete, A. Chiffaudel, F. Daviaud, S. Fauve, P. Odier, and J.-F. Pinton, "Non linear magnetic induction by helical motion in a liquid sodium turbulent flow," Phys. Rev. Lett. **90**, 174501 (2003).
[29]N. O. Weiss, "The expulsion of magnetic flux by eddies," Proc. R. Soc. London, Ser. A **293**, 310 (1966).
[30]P. Odier, J.-F. Pinton, and S. Fauve, "Magnetic induction by coherent vortex motion," Eur. Phys. J. B **16**, 373 (2000).
[31]F. H. Busse, "Magnetohydrodynamics of the Earth's Dynamo," Annu. Rev. Fluid Mech. **10**, 435 (1978).
[32]P. H. Roberts and A. M. Soward, "Dynamo theory," Annu. Rev. Fluid Mech. **24**, 459 (1992).
[33]J. Aubert and J. Wicht, "Axial vs. equatorial dipolar dynamos models with implications for planetary magnetic fields," Earth Planet. Sci. Lett. **221**, 409 (2004).
[34]M. Berhanu, R. Monchaux, S. Fauve, N. Mordant, F. Pétrélis, A. Chiffaudel, F. Daviaud, B. Dubrulle, L. Marié, F. Ravelet, M. Bourgoin, Ph. Odier, J.-F. Pinton, and R. Volk, "Magnetic field reversals in an experimental turbulent dynamo," Europhys. Lett. **77**, 59001 (2007).
[35]N. Schaeffer and P. Cardin, "Quasi-geostrophic kinematic dynamos at low magnetic Prandtl number," Earth Planet. Sci. Lett. **245**, 595 (2006).
[36]M. Bourgoin, R. Volk, P. Frick, S. Kripechenko, P. Odier, and J.-F. Pinton, "Induction mechanisms in von Kármán swirling flows of liquid gallium," Magnetohydrodynamics **40**, 3 (2004).
[37]H.-C. Nataf and J. Sommeria, *La physique et la Terre* (Éditions Belin, CNRS éditions, Paris, 2000).
[38]N. Gilet, Ph.D. thesis, Université Joseph Fourier, Grenoble 1 (2004).
[39]J. Aubert, Ph.D. thesis, Université Joseph-Fourier, Grenoble 1 (2001).
[40]H-C. Nataf, T. Alboussire, D. Brito, P. Cardin, N. Gagnire, D. Jault, J-P. Masson, and D. Schmitt, "Experimental study of super-rotation in a magnetostrophic spherical Couette flow," Geophys. Astrophys. Fluid Dyn. **100**, 281, DOI: 10.1080/03091920600718426 (2006).
[41]P. L. MacFadden and R. T. Merrill, "Fundamental transitions in the geodynamo as suggested by paleomagnetic data," Phys. Earth Planet. Inter. **91**, 253 (1995).